Effect of Fracture Geometry on Well Production in Hydraulic-Fractured Tight Oil Reservoirs

Menglu Lin and **Shengnan Chen,** University of Calgary; **Wei Ding,** RIPED; **Zhangxin Chen** and **Jinze Xu,** University of Calgary

Summary

Tight oil production is emerging as an important new source of energy supply and has reversed a decline in US crude-oil production and western Canadian light-oil production. At present, the combination of the multistage hydraulic fracturing and horizontal wells has become a widely used technology in stimulating tight oil reservoirs. However, the ideal planar fractures used in the reservoir simulation are simplified excessively. Effects of some key fracture properties (e.g., fracture-geometry distributions and the permeability variations) are not usually taken into consideration during the simulation. Oversimplified fractures in the reservoir model may fail to represent the complex fractures in reality, leading to significant errors in forecasting the reservoir performance. In this paper, we examined the different fracture-geometry distributions and discussed the effects of geometry distribution on well production further. All fracture-geometry scenarios were confined by microseismic-mapping data. To make the result more reliable and relevant, a geomodel was first constructed for a tight oil block in Willesden Green oil field in Alberta, Canada. The simulation model was then generated on the basis of the geomodel and history matched to the production history of vertical production wells. A horizontal well was drilled in the simulation model, and different fracture-geometry scenarios were analyzed. Results indicated that the simulation results of simple planar fractures overestimated the oil rate and led to higher oil recoveries. In addition, if the secondary fracture can achieve the same permeability as the main fracture, a hydraulic fracture with branches can increase the well production (e.g., Scenario 2 under the conductivity ratio of 1:2) because of a larger effective contact area between matrix and fracture. Secondary fractures with low permeability can decrease the well productivity compared with wells with biwing planar fractures. Furthermore, the effect of hydraulic-fracture geometries on the cumulative production of the wells with higher main-fracture conductivity was more significant compared with those with lower main-fracture conductivity.

Introduction

Tight oil plays in the western Canadian sedimentary basin have recently experienced a significant increase in activity through advances in horizontal drilling and fracturing technology (Kabir et al. 2011; Legrand et al. 2011; Priyantoro et al. 2012). The Cardium formation in the Pembina field of Alberta is an example of a reservoir where 454 multistage fracture-stimulated horizontal wells were rig released in 2011; use of horizontal wells with multistage hydraulic-fracturing technology has breathed new life into sustainable development of these plays, where hydraulic fractures provide high-permeablity conduits, improve reservoir percolation ability, and increase the drainage area and the oil recovery.

Much research has been conducted on flow regimes (Siavoshi and Bahrami 2013), primary recovery and enhanced oil recovery (Ghaderi et al. 2011; Iwere et al. 2012), reservoir modelling (Wang et al. 2013), and stimulation optimization (Woo et al. 2011) in hydraulic-fractured tight oil reservoirs using reservoir-simulation methods. However, in these works, different hydraulic-fracture geometries are not taken into consideration. Hydraulic fractures are represented by parallel planes that are vertical to the horizontal well. In reality, the geometry of hydraulic fractures can be complex. For example, a hydraulic fracture diverted into the natural fracture can advance either by continued growth in the natural fracture or by kicking out of the natural fracture into the formation rock (Dahi Taleghani and Olson 2014). In layered sedimentary rocks, opening-mode fractures have been observed to abut against bedding contacts, causing fractures to terminate (abutment) at contacts or step over at bedding contacts (Cooke and Underwood 2001). Microseismic-monitoring technology has been used to study the fracture geometry (Quirk et al. 2012; Liu et al 2006; Fischer et al. 2008). But these studies do not integrate the fracture-geometry distribution into the reservoir-simulation process. Stalgorova and Mattar (2012, 2013) proposed analytical models for horizontal wells with multiple fractures. However, numerous assumptions have to be made in order to apply the analytical models in practice. In this study, we first used Petrel to construct a geological model for an actual block in the Cardium formation of Willesden Green oil field in Alberta, Canada. CMG IMEX (CMG 2013) was then employed to construct a dynamic simulation model based on the geological model before history matching was conducted. Local grid refinement were generated near the hydraulic fractures. Microseismic data was used to confine and describe the characteristics of hydraulic fractures in tight oil reservoirs. Finally, horizontal wells with different fracture geometries and conductivities were simulated and compared.

Geological Model. The Cardium formation consists of interbedded sandstone, shale, and some local conglomerate, which spreads over much of western Alberta (Krause et al. 1994). Oil production in Cardium started more than 50 years ago, and activities in the tight formations in Cardium began in 2005. The Willesden Green oil field is located in south-central Alberta, and covers an area of 50,827 ha (Varga et al. 2007). In Willesden Green field **(Fig. 1),** the average vertical depth of the formation is 1900 to 2300 m and the formation has a significant amount of solution gas. The net pay thickness is 5 to 18 m, resulting in large original oil in place (Mageau et. al. 2012).

To build the geological model, a block with two vertical production wells, one horizontal production well, and one observation well was selected. Structural surfaces are built on the basis of well tops where three horizons (the CARD, CARDSD, and BLACKSTN) are generated. These three horizons include the interval of CARD and CARDSD formation. The horizontal well is at the top of CARDSD formation, which can be observed in **Fig. 2.** Vertical wells produce from the CARDSD zone, and the stimulated horizontal well produces from both the CARD and the CARDSD zone. Because the reservoir is not supported by aquifer or gas cap, solution-gas drive is the main driving force. The length of the model is 1770 m and the width is 810 m. The model consists of 143,370 grids. The properties (e.g., matrix permeability and porosity) are derived from sequential Gaussian simulation

This paper (SPE 167761) was accepted for presentation at the SPE/EAGE European Unconventional Resources Conference and Exhibition, Vienna, Austria, 25–27 February 2014, and revised for publication. Original manuscript received for review 22 October 2013. Revised manuscript received for review 30 January 2015. Paper peer approved 13 April 2015.

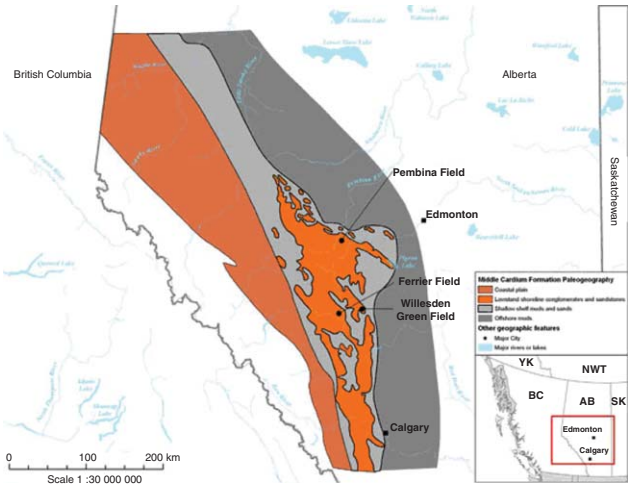

Fig. 1—Location of Willesden Green oil field (Source: National Energy Board).

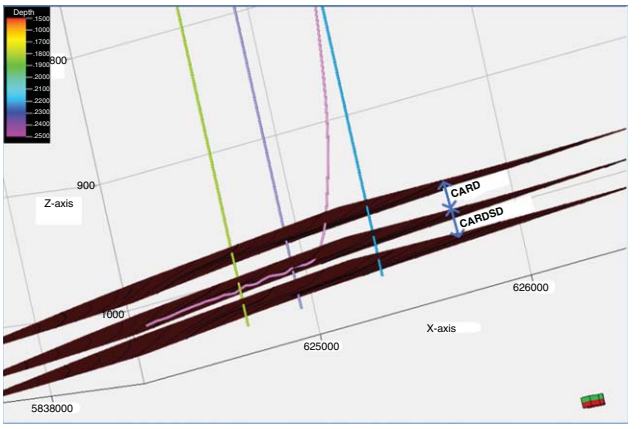

Fig. 2—Three horizons and well locations.

using the core data, as shown in **Fig. 3.** Specifically, the matrix horizontal permeability ranges from 0.06 to 0.94 md, with an average value of 0.2 md. Matrix vertical permeability is 1/10 of the horizontal value, and the porosity range in the model is between 7.8 and 15%.

Numerical-Simulation Model. ***Reservoir and Fluid Properties.*** The numerical-simulation model is constructed on the basis of the geological model. Unlike in simulation of shale-gas reservoirs, adsorption effect is not considered in this model because such an effect is not significant in tight oil reservoirs equally. The effect of non-Darcy fluid flow is examined. Because liquid-flow rate is relatively lower compared with gas-flow rate in hydraulic fractures in shale-gas formations, the non-Darcy effect on oil cumulative production rate is insignificant. Details are presented in the Results and Discussion section. The geological model constructed by Petrel is exported directly into CMG IMEX (CMG 2013). There are 177 grids in the *i*-direction, 81 grids in the *j*-direction, and 10 grids in the *k*-direction. In the *k*-direction, there are 10 layers where the CARD formation consists of five layers (Layers 1 through 5). The CARDSD formation includes the Layers 6 through 10. The grid size of *i*- and *j*-directions is 10 m. The grid top ranges from 1945 to 1988 m. Properties of the tight oil formation and reservoir oil properties are all obtained from field data, as shown in **Table 1.**

Relative Permeability Curves and Initial Condition. The initial pressure of each gridblock is determined by a reference pressure and a reference depth, as shown in Table 1. The water/oil and gas/oil contacts have been set outside the boundary of the reservoir model because there are no signs of a bottomwater zone and the reservoir initial pressure is higher than the bubblepoint pressure (i.e., no gas cap). The initial phase saturations are imposed as the endpoint saturations in the relative permeability curves. Relative permeability curves are obtained from two reference papers (Ghaderi et al. 2011; Ghaderi et al. 2012) on the Cardium tight formation and tuned further to match the production history of the two vertical wells, as depicted in **Fig. 4.** Oil-wet, mixed-wet, and water-wet rock wettability have all been found in the Cardium formation. In our simulation model, based on the history-matching results, the reservoir rock is likely to be water-wet, which is in accordance with the reference papers. In this situation, no transition zone is assumed to exist in the reservoir. A test run is performed for 5 years without source/sink terms (i.e., injectors/producers), and no pressure and saturation changes are observed, which implied that the model reached the equilibrium state.

Hydraulic Fracture—Local Grid Refinement. In any reservoir simulator, it is a challenging task to simulate the actual width and permeability of a hydraulic fracture because of the high computational cost and the convergence issue. Alternatively, grids with an equivalent permeability and width are used to represent the fracture in the simulator. It is assumed that conductivity of an actual hydraulic fracture is equal to that of the pseudoized fracture block in the model (Rubin 2010).

$$k_f \times w_f = k_e \times w_{\text{block}}. \quad \ldots\ldots\ldots\ldots\ldots\ldots\ldots\ldots \quad (1)$$

For example, if the fracture width is 10 mm and the actual fracture permeability is 15 darcies; fracture conductivity, which is the product of the fracture permeability and width, is 150 darcy·mm. If the grid width representing the hydraulic fracture in the model is 60 cm, then the effective permeability in the gridblock representing the hydraulic fracture can be calculated as

$$k_e = \frac{k_f \times w_f}{w_{\text{block}}} = \frac{15{,}000\,\text{md} \times 0.01\,\text{m}}{0.6\,\text{m}} = 250\,\text{md} \quad \ldots\ldots \quad (2)$$

A magnified plot of the local grid refinement of a hydraulic fracture is shown in **Fig. 5.** Gridblocks in the middle represent

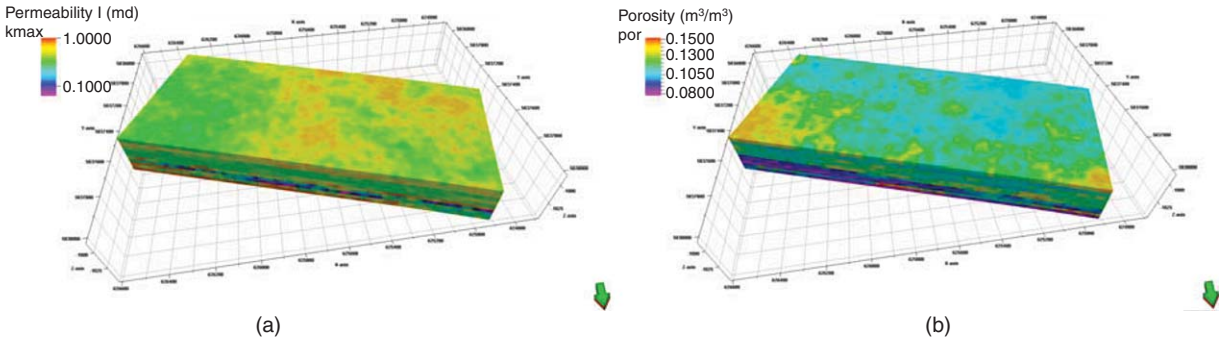

Fig. 3—Properties of geological model. (a) Matrix permeability of geological model. (b) Matrix porosity of geological model.

Reservoir temperature (°C)	65
Bubblepoint pressure (MPa)	22.8
Oil density at stock-tank condition (°API)	30
Gas density at stock-tank condition (air=1)	0.776
Formation compressibility (kPa^{-1})	6.41×10^{-7}
Total compressibility (kPa^{-1})	2.28×10^{-5}
Reference pressure (kPa^{-1})	26 880.7
Reference depth (m)	2010
Water/oil contact (m)	2040
Solution-gas/oil ratio at 23 MPa (std m^3/std m^3)	185
Average production gas/oil ratio (std m^3/std m^3)	1470

Table 1—Properties of formation and reservoir fluid.

the hydraulic fracture. The width of the pseudoized fracture grid is 2 ft.

History Matching. Three producers (one horizontal well and two vertical wells) are simulated in the numerical model. Wells 1 and 2 are two vertical producers, which have been producing since February 1968 and September 1976, respectively. The history-matching process was performed such that the oil rates were applied as constraints and gas rates of the two vertical wells were matched. A pressure-buildup test of Well 1 was conducted on 15 July 2009, and the average reservoir pressure was measured to be 22.8 MPa. This pressure-buildup test was performed in order to obtain the formation pressure before drilling the horizontal well. Unfortunately, the well flowing bottomhole pressure (BHP) was not reported and water production was negligible because of the primary production and unconnected aquifers. The oil rates of the two vertical wells are used as inputs (shown in **Fig. 6**) and the simulated average pressure is 21.6 MPa. The simulated gas rates of the two vertical wells are shown in **Fig. 7.** In addition, our model can be regarded as a "conceptual" model with realistic data collected from the field. Well 3 is a newly drilled horizontal well with multistage hydraulic fractures. Confined by the microseismic-mapping data, different fracture-geometry scenarios are simulated along the horizontal well. The effect of the hydraulic-fracture geometries on the cumulative oil production is analyzed, and sensitivity analysis of fracture conductivity is performed for various fracturing scenarios. Minimum BHP of the horizontal well is kept at 7 MPa.

Microseismic Data. Microseismic imaging is a monitoring technique that is used in the oil and gas industry to monitor and map fracture geometries created by hydraulic-fracturing stimulations. A microseismic event occurs when the rock beneath the ground surface fails (Mohammad and Miskimins 2012). Data collected during well stimulations in tight shale reveal generally a wide spread of microseismic events, as shown in **Fig. 8.** In this figure, there are microseismic events from eight stages. The fracture half-lengths and heights are not constant values, and half-lengths on both sides of every stage are not symmetrical. On the basis of the map, it can be observed that the event cloud shows a clear orientation, yet still covers a significantly wider area than the hydraulic-fracture geometry. In many reservoirs, propagation of the hydraulic fractures may be complex because of interaction with pre-existing natural fractures, fissures, and other geologic heterogeneities (Cipolla et al. 2008; Mayerhofer et al. 2008; Potluri et al. 2005). In addition, complex fracture geometries may be created when there is no significant difference between the minimum and maximum principal stresses in the reservoir (Fan et al. 2010). **Fig. 9** depicts a microseismic map from one stage of the horizontal well. When a complex fracture network is expected in the formation, it is still not mpossible to predict an exact fracture-network geometry in the area of the event cloud. In this study, multiple different cases of geometry of hydraulic fractures, ranging from simple planar fractures to complex fractures, are studied in reservoir simulation, which is demonstrated in Fig. 9. These geometries represent Scenario 1 (planar fracture), Scenario 2 (branched fracture), and Scenario 3 (complex fracture). In our model, four fracture half-lengths ranging from 100 to 250 m are simulated, and fracture height is the same as the height of the oil zone.

Hydraulic-Fracture-Geometry Scenarios. Local refinement grids are used to represent hydraulic fractures in the simulation model. The horizontal length of Well 3 is 1000 m. The 1000-m lateral, which is in Layer 6, is completed with five stages, and fracture spacing is 200 m. The fracture height is equal to vertical height of the simulation model. It is assumed that the horizontal well is drilled along the direction of minimum horizontal stress.

As already mentioned, propagation of a hydraulic fracture may be complex because of the interaction with pre-existing natural fractures, fissures, cleavage, and rock-mechanical heterogeneities. Three different hydraulic fractures are modelled. In the first scenario, the hydraulic fractures are ideal parallel planar fractures. In the second scenario, branches are added to the planar fractures. In the third scenario, complex hydraulic fractures are modelled according to the characteristics of the microseismic-events cloud. Sensitivity of fracture half-length, fracture conductivity, and fracture-geometry distribution is analyzed. For all three scenarios, a no-flow boundary is assumed and BHP of the horizontal well is set to 7 MPa. The average reservoir pressure has dropped to below the bubblepoint pressure when the horizontal well is put into production.

Scenario 1. In Scenario 1, we assume the transverse hydraulic fractures propagate symmetrically in a plane perpendicular along the minimum principal stress. Ideal planar fractures are modelled, and the 1000-m lateral is completed with five parallel identical fractures **(Fig. 10).** The grid-top value is calculated by the well's

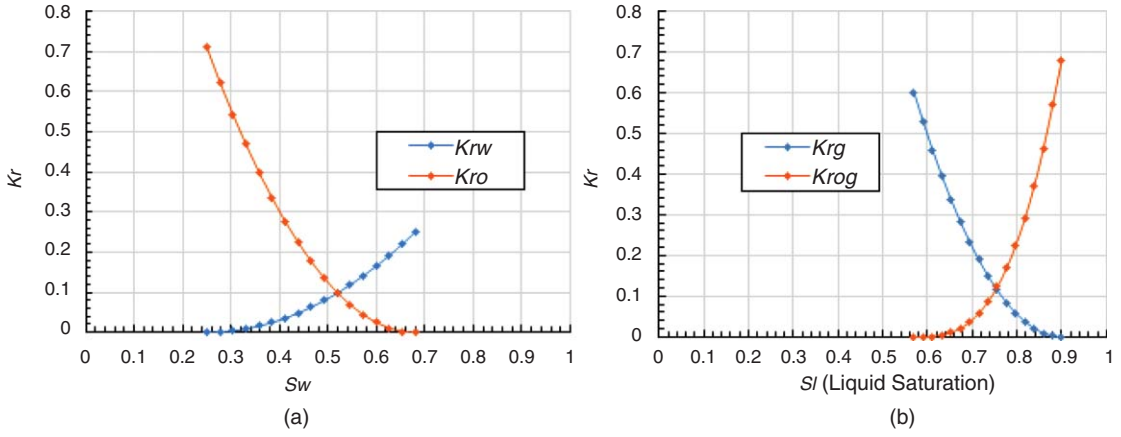

Fig. 4—Relative permeability curves. (a) Oil and water relative permeability curve and (b) liquid and gas relative permeability curve.

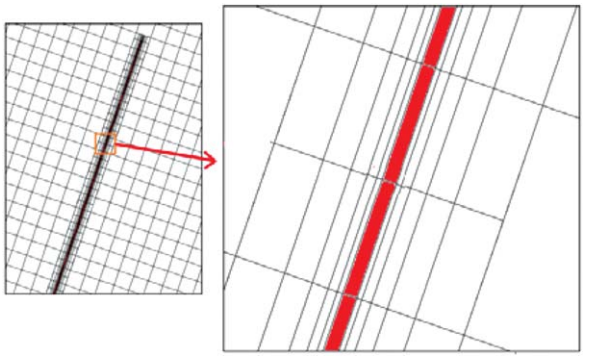

Fig. 5—Magnified picture on local refined grids at and near the hydraulic fracture.

true vertical depth subsea. According to Bazan et al. (2013), a fracture with dimensionless conductivity higher than 10 should be targeted while designing a stimulation job and such a fracture is close to infinite conductivity. However, it should be noted that the effective fracture conductivity in the reservoir can be as significant as 90% lower than their laboratory-measured values because of the effects of multiphase flow, proppant embedment, and uneven proppant concentration (Palisch et al. 2007). In our model, four fracture conductivities of 100, 150, 200, and 500 darcy·mm are examined. The fracture width is assumed to be 10 mm, and thus the values of fracture permeability are between 10 and 50 darcies, respectively. Four fracture half-lengths of 100, 150, 200, and 250 m, are also studied.

Scenario 2. In this scenario, branches are added to the planar hydraulic fractures, which are shown in **Fig. 11.** For Scenarios 1 and 2, the total fracture volume (summation of all fractures) is kept the same, which can be estimated by the usage (and flowback) data of the fracturing fluid and proppant. Secondary fractures are created typically by activating the pre-existing natural fractures, and thus they are likely to be narrower than the main hydraulic fractures. In this study, the width of a secondary fracture is assumed to be half that of the main fracture width. Further, the width of a tertiary fracture (located at the tip of each branch) will be half of the width of a secondary fracture, which makes it a quarter of that of the main fracture. It should be noted that, as the total fracture volume is the same for Scenarios 1 and 2, adding secondary and tertiary fractures in Scenario 2 implies the length for main fracture is decreased accordingly.

In addition, if the secondary fractures are propped well, permeability of the secondary fracture may be close to that of the main fracture. Otherwise, if secondary fractures are not well-propped because of the narrow width and/or severe proppant crush/embedment, permeability of such a fracture can be less than that of the main fracture. In this study, two secondary fracture permeabilities are analyzed—its value to be equal and one-quarter of the main fracture permeability, making the secondary-/main-fracture conductivity ratio 1:2 and 1:8. At the same time, four cases with main-fracture conductivity values of 100, 150, 200, and 500 darcy·mm are simulated, respectively. If the secondary-fracture permeability is the same as that of the main fracture, corresponding conductivities of the secondary fractures are 50, 75, 100, and 250 darcy·mm. If the secondary-fracture permeability is one-quarter of the main-fracture permeability, conductivity of secondary fractures are 12.5, 18.75, 25, and 62.5 darcy·mm.

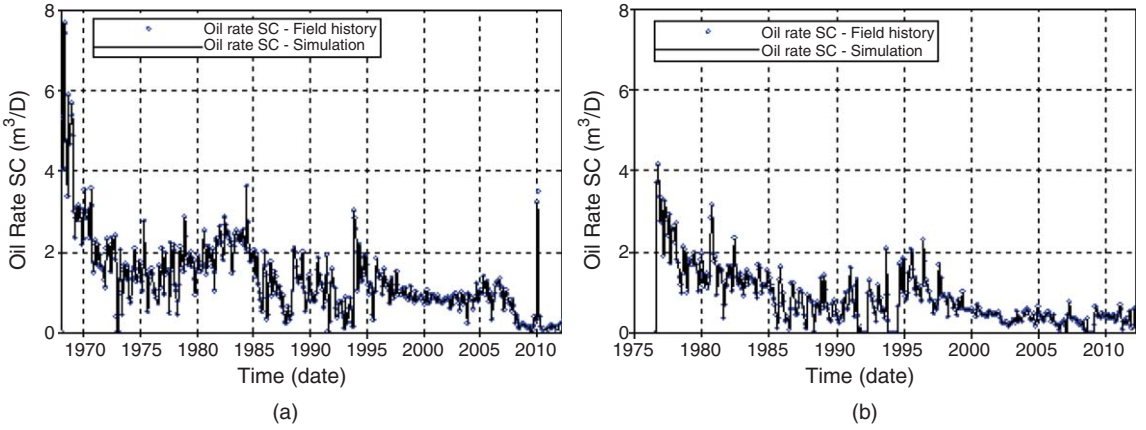

Fig. 6—Oil production (constraints) of two vertical wells. (a) Oil rate of Well 1. (b). Oil rate of Well 2.

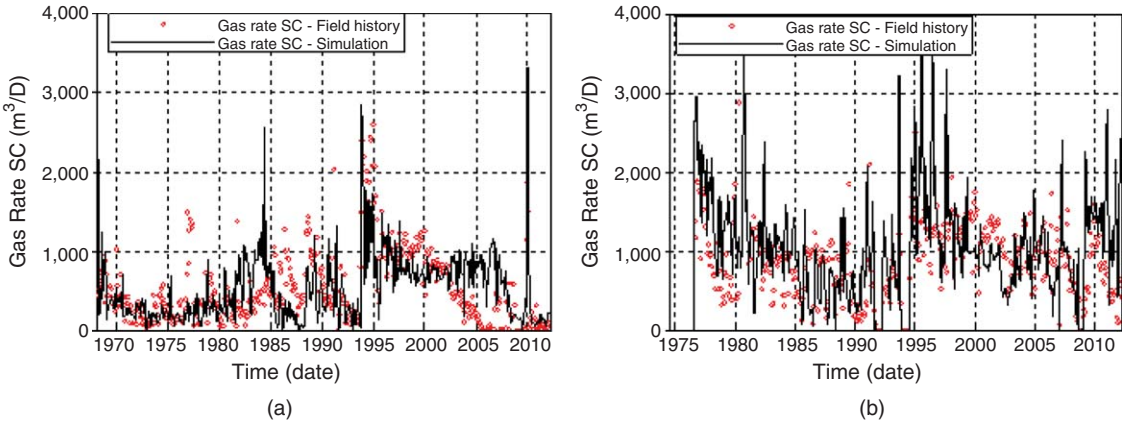

Fig. 7—History-matched gas production rates of two vertical wells. (a) Simulated gas rate of Well 1. (b) Simulated gas rate of Well 2.

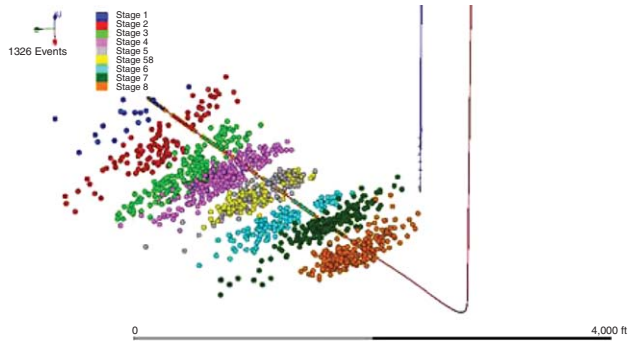

Fig. 8—Different stages of the microseismic-event view of a horizontal well.

Scenario 3. In Scenario 3, geometry of the hydraulic fractures is more complex to account for the interaction with fissures and natural fractures, as shown in **Fig. 12.** There are three different directions a hydraulic fracture could propagate when encountering a closed and cemented natural fracture. (1) The natural fracture may have no influence, and the hydraulic fracture propagates in the plane without interruption. The fracture crossover may be because of the high-strength cement (comparable to matrix) or fracturing pressure being lower than the normal stress perpendicular to natural fracture. (2) The hydraulic fracture is deflected, and the fluid is diverted completely into a natural-fracture system. (3) The natural fracture stops or at least slows down hydraulic-fracture growth in the presence of high stress anisotropy and enhanced leakoff (Dahi Taleghani and Olson 2014). In addition, hydraulic fractures with complexity also tend to be created when there is no significant difference between the maximum and minimum principal horizontal stress. Total fracture volume of Scenario 3 is again kept the same as the volume in Scenarios 1 and 2. More secondary and tertiary fractures are added in Scenario 3 to represent a complex fracture network. Thus, length of the main fracture in Scenario 3 is the shortest among all three scenarios. Similar to Scenario 2, two secondary-/main-fracture permeability ratios of 1:1 and 1:4 (i.e., secondary-/main-fracture conductivity ratios of 1:2 and 1:8) are simulated. Different main-fracture-conductivity values of 100, 150, 200, and 500 darcy·mm are simulated for Scenario 3, respectively.

Results and Discussion

The Effect of Non-Darcy Flow in Hydraulic Fractures. Non-Darcy-flow effects were simulated in the high-conductivity hydraulic fractures and results are shown in **Fig. 13.** It can be observed that there was no noticeable difference between the oil rates with and without non-Darcy-flow effects (Fig. 13a), while slight differences were found in the corresponding gas-production rates, as shown in Fig. 13b. In addition, the Reynolds number was examined to confirm that non-Darcy flow did not exist in the liquid flow in the hydraulic fractures. The Reynolds numbers of all the scenarios were calculated, and results showed that for the highest Reynolds number, oil flow was 1.02 and that for gas was 18.30. Different critical Reynolds numbers for non-Darcy flow have been reported in the literature (Bear 1972; Hassanizadeh and Gray 1987; Blick and Civan 1988), ranging from 3 to 100. Thus, non-Darcy flow was not expected for oil flow but may appear in gas flow, which was in accordance with simulation results.

Ideal Planar Fractures—Effect of Main-Fracture Length and Conductivity. Effects of the half-length and conductivities of the main fractures are examined first in this study. The cumulative oil productions of Scenario 1 with four different fracture half-lengths (i.e., 100, 150, 200, and 250 m) and four different conductivities (100, 150, 200, and 500 darcy·mm) are plotted in **Fig. 14.** It can be observed that, the larger the fracture half-length under the same conductivity, the higher cumulative oil production. Similarly, for the same fracture half-length, the higher the fracture conductivity, the higher cumulative oil production, especially during the first 2 years. The difference amongst different fracture

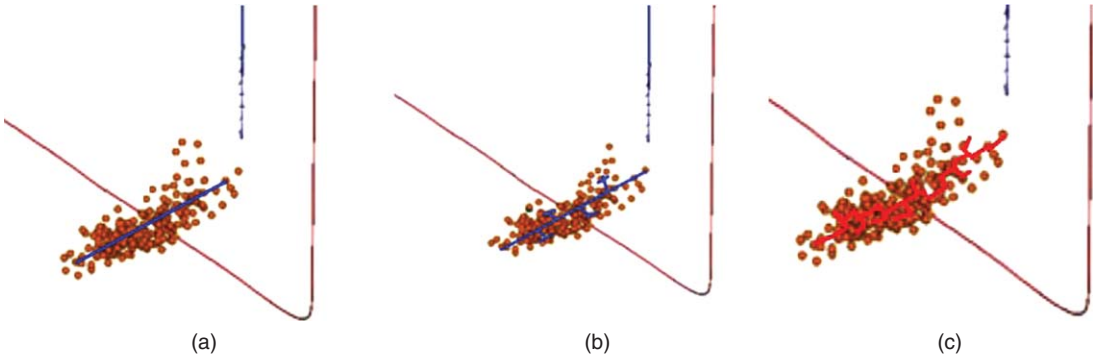

Fig. 9—Different fracture geometries in microseismic-data map.

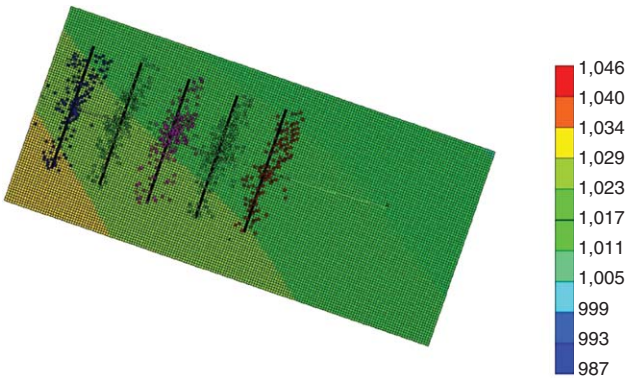

Fig. 10—Scenario 1 with ideal biwing planar fractures.

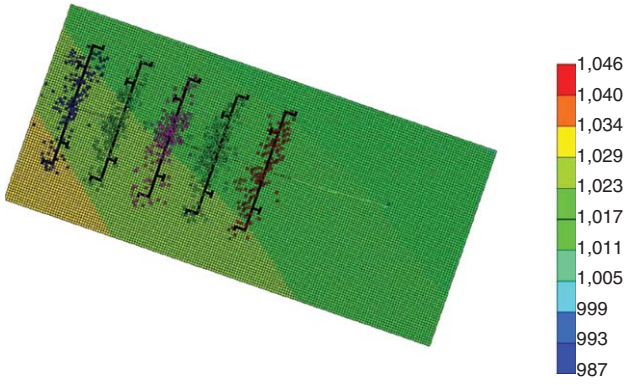

Fig. 11—Scenario 2 with two branches in planar fractures.

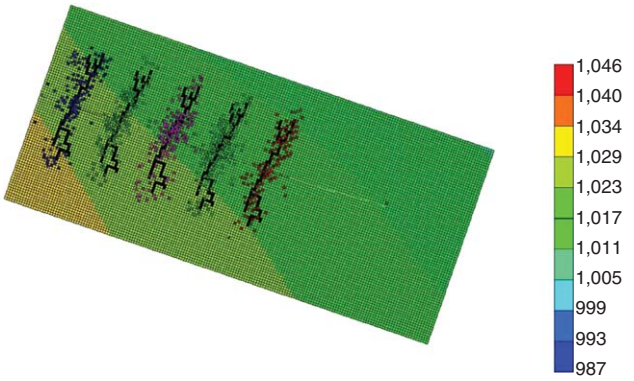

Fig. 12—Scenario 3 with complex fractures.

half-lengths is smaller under low fracture conductivity. For example, when fracture conductivity is 100 darcy.mm, cumulative oil production at the 1,825th day (fifth year) is increased by 31.7% (13 000 m^3) when fracture half-length increases from 100 to 250 m, and its value increased by 52.3% (23 000 m^3) when fracture conductivity is 500 darcy·mm. It can also be observed from Fig. 14 that the differences amongst different conductivities increases as production time proceeds, and reaches a peak value in the fifth year and then differences become relatively smaller during later production. If one wants to increase the early production rate, hydraulic fractures with high conductivity are needed. For example, when fracture half-length is 250 m, the first year's production will be increased by 73.6% if fracture conductivity is increased from 100 to 500 darcy·mm.

Effect of Fracture Geometry. Cumulative oil production for three scenarios with different fracture conductivities is simulated and shown in **Fig. 15.** Permeability of the secondary fracture is assumed to be a quarter of that of the main fracture for Scenarios 2 and 3. Because secondary fractures are significantly narrower compared with the main fracture and have uneven proppant distribution, crush and embedment in the secondary fractures are more significant than in the main fractures. It can be observed that cumulative-production values differ slightly among three scenarios in the first 180 days, but the difference increases as production proceeds and the main-fracture conductivity increases. At the end of the 10th year, cumulative production of Scenario 3 with complex fractures is 15% less than that of Scenario 1 with ideal parallel planar fractures. This implies that simulations using parallel planar fractures overestimate the well productivity when a fracture network is created in tight oil formations. Because of the reduction of secondary-fracture conductivity, these fractures cannot transport reservoir fluids to the main fracture and wellbore effectively. Taking the case with conductivity of 500 darcy·mm for example, when the main fracture is 500 darcy·mm, the dimensionless fracture conductivity is 25, which can be regarded as infinite conductivity (Bazan et al. 2013). However, the dimensionless conductivity of the secondary fracture is reduced to approximately 3. Secondary fractures with low-conductivity values are noneffective to transport the fluids. In addition, because the total fracture volumes are kept the same, the main fracture half-length of Scenarios 2 and 3 is shorter than that of Scenario 1, even though the contact area between matrix and fracture is increased. **Fig. 16** depicts the reservoir-pressure distribution after 10 years of production. It can be observed that complex fracture scenarios with finite conductivity limit the pressure conduction. Even though the contact area of a complex fracture with matrix increases significantly, the qualities of the subfractures become poor. In other words, if complex fractures are targeted to be created in the formation, efforts must be made to guarantee sufficient conductivity of the secondary and tertiary fractures.

Effect of Secondary-Fracture Permeability. In the preceding subsection, secondary-fracture permeability is assumed to be one-quarter of the main-fracture permeability. To analyze its effects on well performance, secondary-fracture permeability is then assigned to be the same as that of the main fracture for Scenarios 2 and 3. Under such circumstance, we assume the secondary fractures are propped well without severe proppant uneven distribution, embedment, and crush. Secondary-fracture width is kept as one-half of that of the main fracture again, which makes the conductivity of secondary to main fracture 1:2. Cumulative production over 10 years for three different fracture geometries is plotted in **Fig. 17.** Unlike previous results with low secondary-fracture permeability, Scenario 2 shows an optimal performance, while Scenario 3 still has the lowest production. Initial production (e.g., at the end of 6 months) among the three scenarios is almost the same, which could be because the reservoir fluids produced for all the scenarios are from the reservoir matrix near the main fractures mainly during early production time. During Years 1 and 6, cumulative production of Scenario 2 is higher than that of Scenario 1, especially under high main-fracture conductivity. The ability of secondary fractures to transmit fluid has improved significantly by keeping the permeability of the main and the secondary fractures the same. Compared with biwing fractures in Scenario 1, fractures in Scenario 2 with branches have larger contact areas between

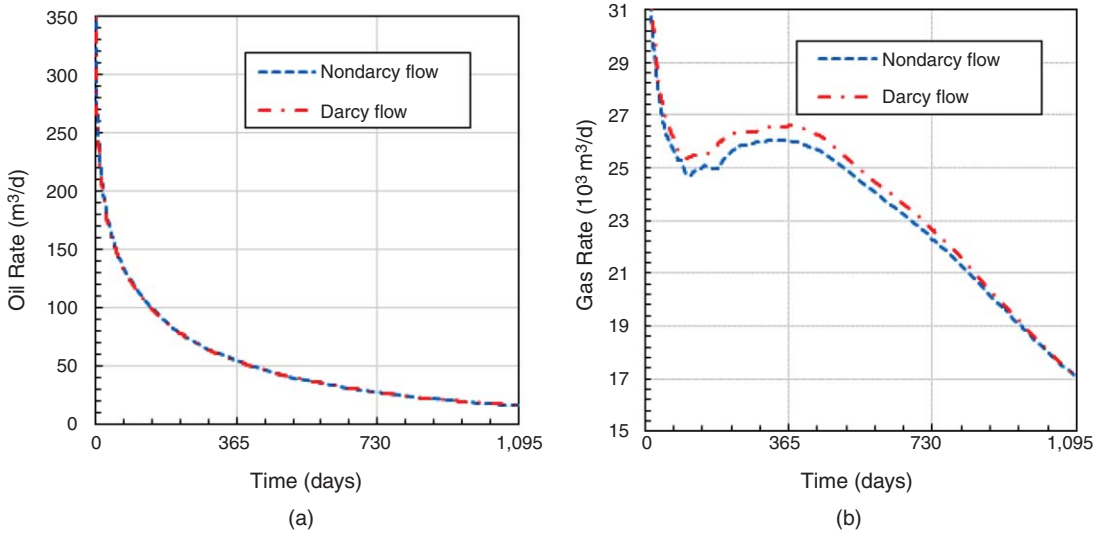

Fig. 13—Comparison of Darcy flow and non-Darcy flow in main fractures with conductivity of 500 darcy·mm. (a) Comparison of Darcy flow and non-Darcy flow for oil phase. (b) Comparison of Darcy flow and non-Darcy flow for gas phase.

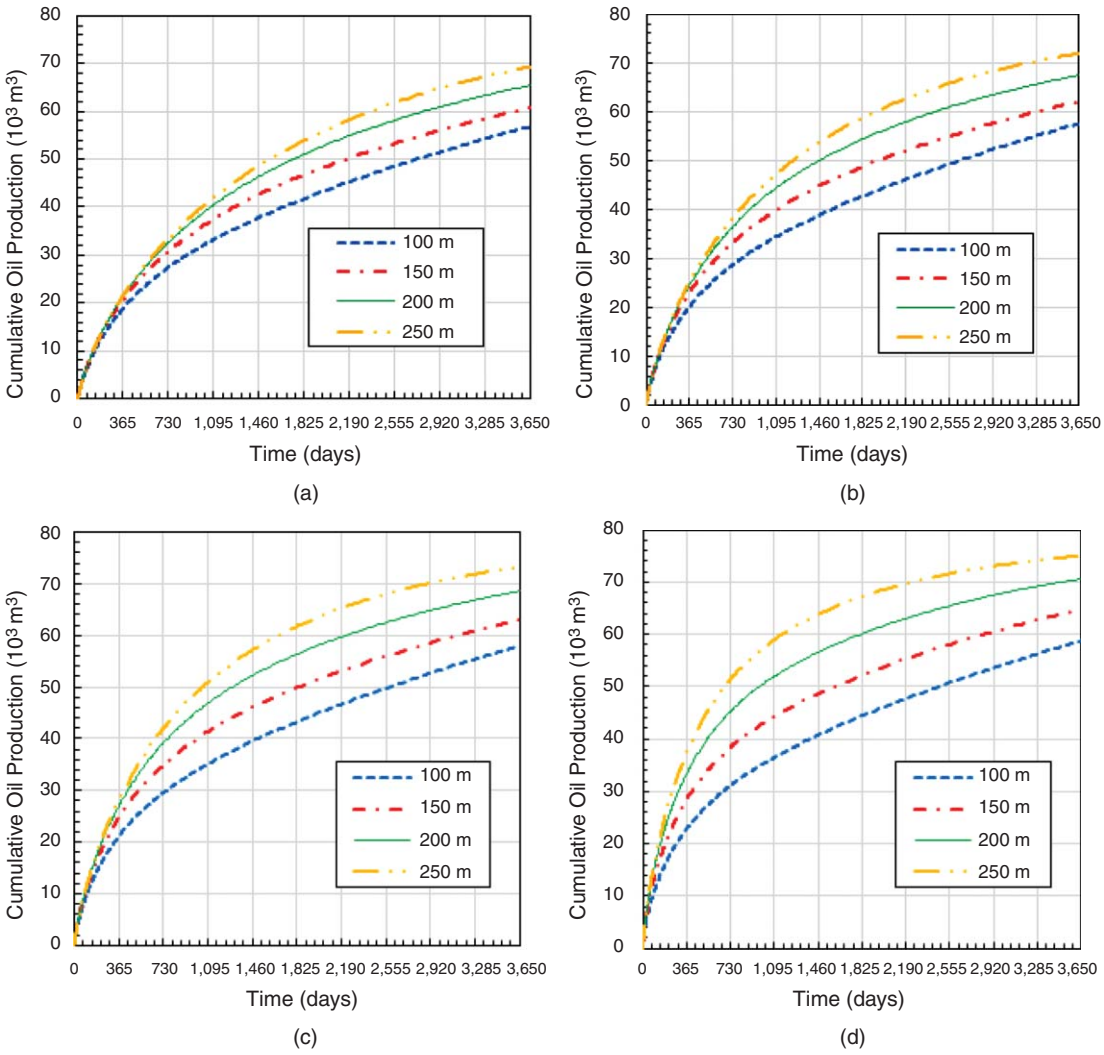

Fig. 14—Cumulative oil production of different fracture half-lengths and conductivities (Scenario 1). (a) Different half-lengths and fracture conductivity at 100 darcy·mm. (b) Different half-lengths and fracture conductivity 150 at darcy·mm. (c) Different half-lengths and fracture conductivity at 200 darcy·mm. (d) Different half-lengths and fracture conductivity at 500 darcy·mm.

matrix and fractures and can also transport all the fluids effectively. In other words, if the effective conductivity of the second fracture can be achieved, it is recommended to add some complexity in fractures. For long-term production, the matrix around the fracture has been depleted and fluids from the matrix in the distance begin to contribute to the production. If main fractures can connect a more-remote reservoir region away from the wellbore—that is, having a longer fracture half-length—well-production rate can be maintained better compared with scenarios with shorter main-fracture half-lengths. Because there are no secondary fractures in Scenario 1, the half-lengths of the mainfractures are the longest. This leads to a highest overall cumulative production rate in 10 years. However, for a more-complicated fracture geometry shown in Scenario 3, cumulative production of 10 years is lower than the other two scenarios. Because the total facture volumes are the same for all three scenarios, well-developed secondary and tertiary fractures in Scenario 3 limit the length of the main fractures, and thus yeild a smaller drainage area. Pressure distributions for different scenarios are shown in **Fig. 18.**

Flow-Regime Analysis. It is important to understand the flow regime caused by the stimulated hydraulic fractures. In this study, the bottomhole pressure of the horizontal well is held constant and the simulated well-production rates are regarded as the production data. For the horizontal well with multiple transverse fractures in a tight reservoir, the straight-line analysis method and a series of diagnostic signatures can be used to analyze the flow regimes (Clarkson 2013a, 2013b). Rate-normalized derivative signature analysis (Song and Ehlig-Economides 2011) is used to identify the flow regime. Rate-normalized pressure (RNP) and its derivative are shown in Eqs. 2 and 3. The horizontal ordinate t_e is material-balance time, shown in Eq. 4.

$$RNP = \frac{P_i - P_{wf}(t)}{q(t)}, \quad \ldots\ldots\ldots\ldots\ldots\ldots\ldots\ldots\ldots\ldots (3)$$

$$RNP' = \frac{\mathrm{d}\,RNP}{\mathrm{d}\,\ln t_e}, \quad \ldots\ldots\ldots\ldots\ldots\ldots\ldots\ldots\ldots\ldots (4)$$

$$t_e = \frac{Q(t)}{q(t)}. \quad \ldots\ldots\ldots\ldots\ldots\ldots\ldots\ldots\ldots\ldots (5)$$

For the RNP derivative signature, a 0.5-slope trend implies a linear-flow regime, a zero-slope trend suggests radial-flow regime, and a unit slope indicates pseudosteady state (dominated by the boundary). As shown in **Fig 19,** pseudolinear flow, early radial flow, compound linear flow, and pseudosteady-state flow can be identified for the fractured horizontal well. Flow regimes of Scenario 1 (biwing fracture) with a half-length of 250 m are shown in Fig 19a. Taking the main fracture conductivity of 100 darcy·mm, pseudolinear flow, which arises at the beginning of the production, lasts for a short time and then the early-radial flow lasts for more than 10 days. These two flow regimes happen before fracture interference occurs. After fracture interference, compound linear flow appears and the fluids flow into the fractures from the reservoir

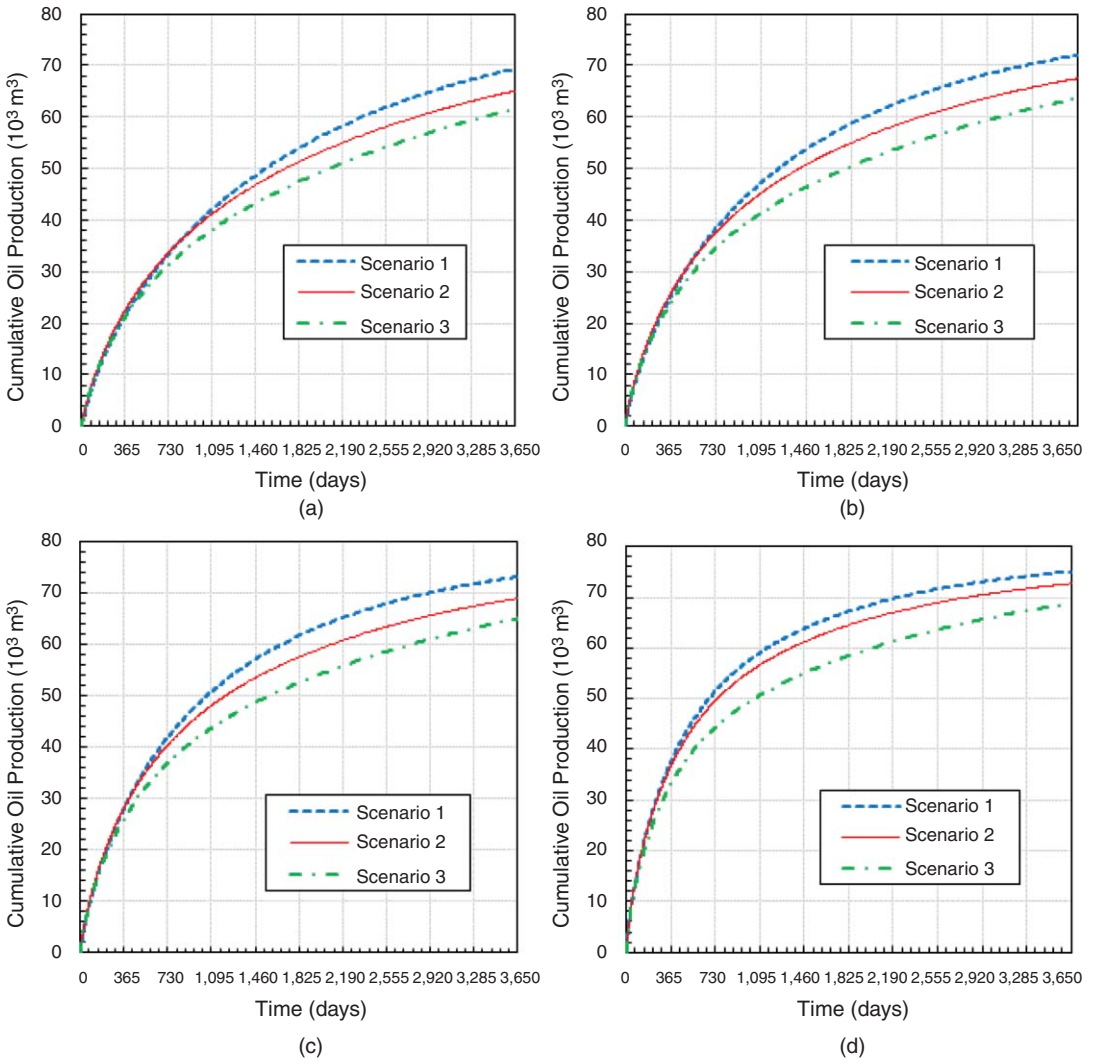

Fig. 15—Cumulative oil production with different fracture conductivity (secondary-/main-fracture permeability ratio of 1:4 and conductivity ratio of 1:8). (a) Fracture conductivity of 100 darcy·mm. (b) Fracture conductivity of 150 darcy·mm. (c) Fracture conductivity of 200 darcy·mm. (d) Fracture conductivity of 500 darcy·mm.

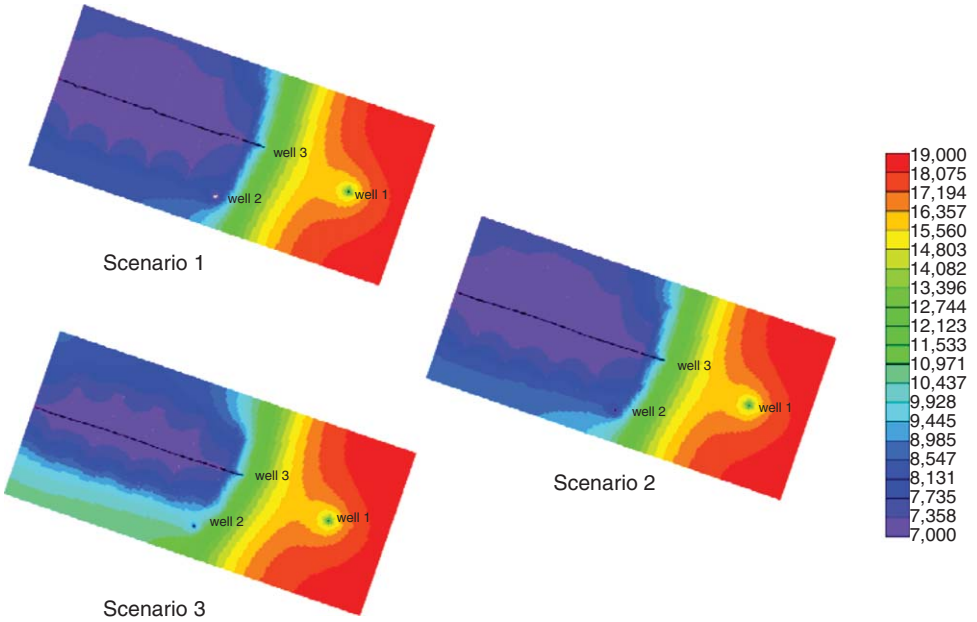

Fig. 16—Pressure distribution after 10 years (main-fracture conductivity is 500 darcy·mm; secondary-/main-fracture permeability ratio is 1:4; and conductivity ratio is 1:8).

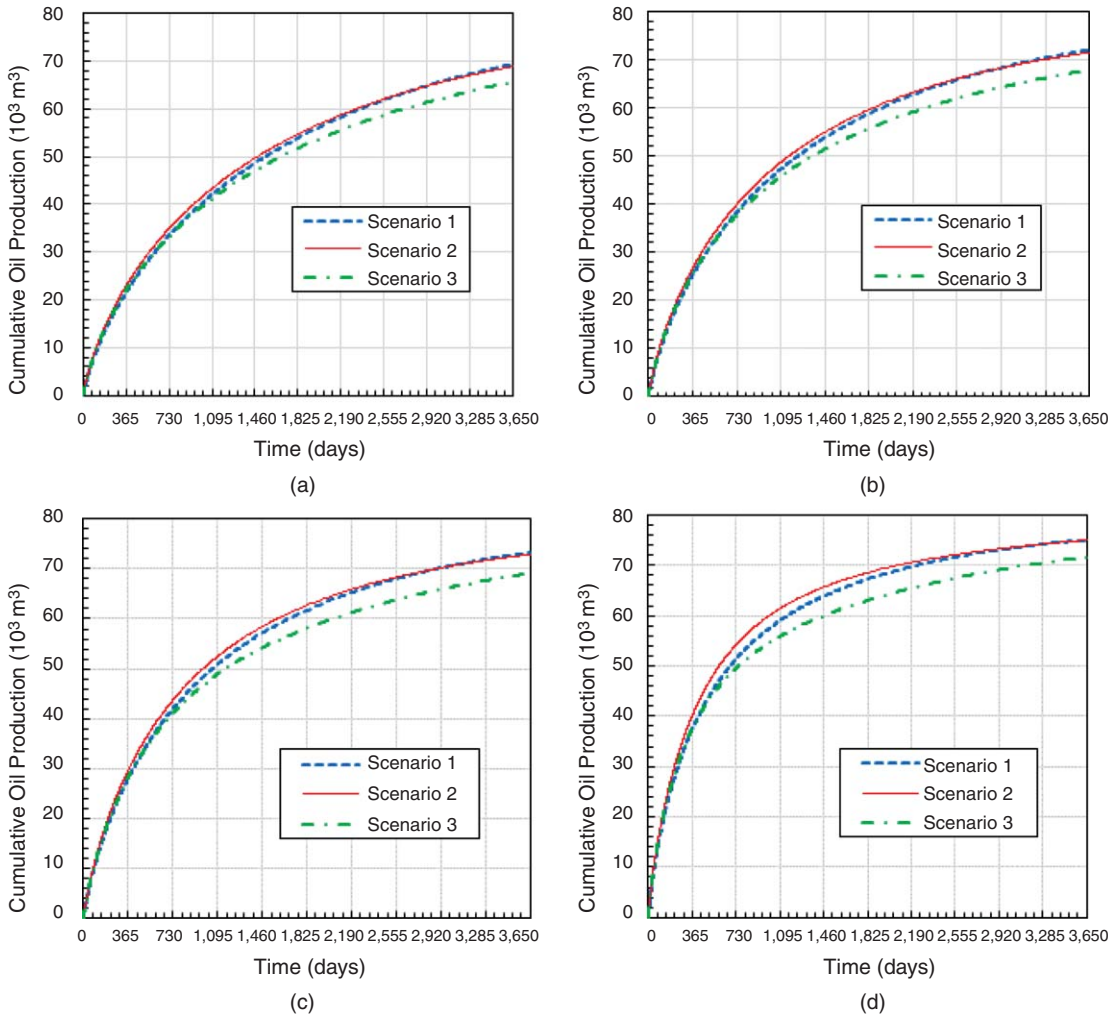

Fig. 17—Cumulative oil production of three scenarios at different fracture conductivities at a ratio of 1:2. (a) Main-fracture conductivity of 100 darcy·mm. (b) Main fracture conductivity of 150 darcy·mm. (c) Main-fracture conductivity of 200 darcy·mm. (d) Main-fracture conductivity of 500 darcy·mm.

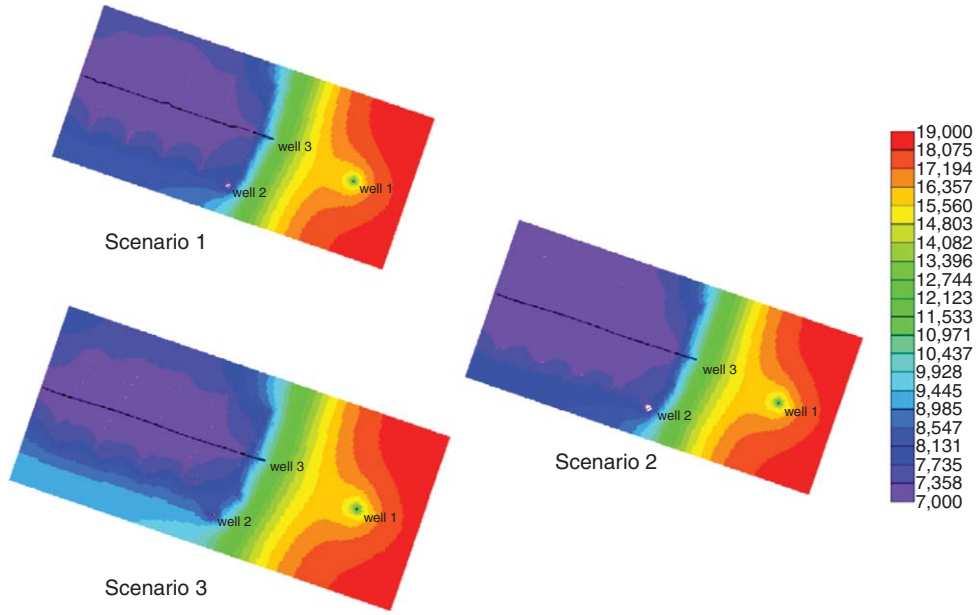

Fig. 18—Pressure distribution after 10 years at 500 darcy·mm and a ratio of 1:2.

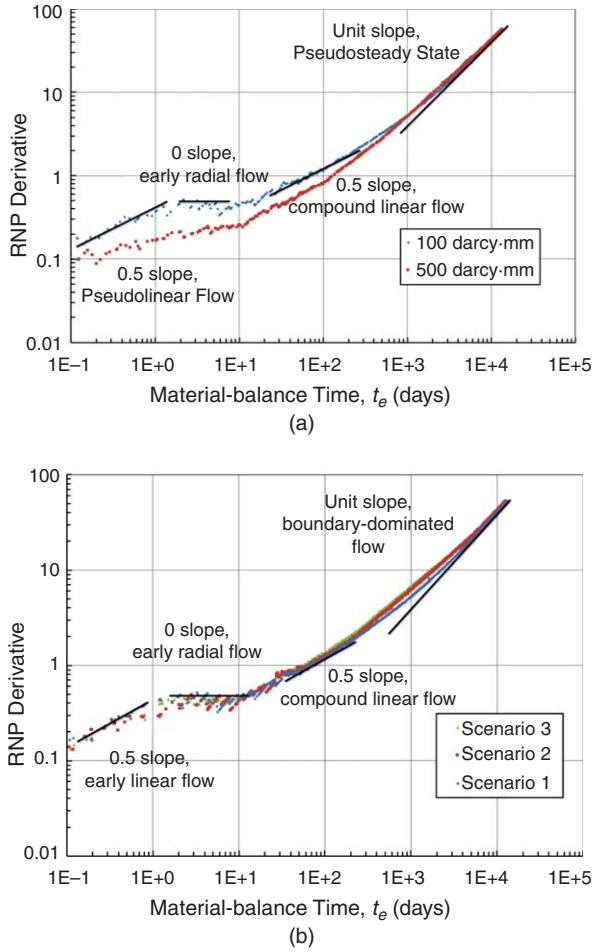

Fig. 19—Rate-normalized pressure (RNP) and its derivative signature for the horizontal well with multiple stage fractures. (a) RNP derivative signature for biwing fracture (Scenario 1). (b) RNP derivative signature for three scenarios (fracture conductivity of 500 darcy·mm).

matrix beyond the fracture tip. Finally, pseudosteady-state-flow dominates the fluid flow in the middle and late period. As fracture conductivity increases, time for flow regime to change becomes relatively earlier. The pseudosteady-state flow regime resulting from fracture interference (observed as a nearly unit slope) and late pseudoradial flow (observed as a zero slope) do not appear in the horizontal well. It may be caused by a large fracture spacing and short distance from fracture tip to the reservoir boundary.

Fig. 19b depicts flow regimes of different fracture geometries, and similar flow regimes are shown in terms of RNP derivative signatures. Similarly, early linear flow and early radial flow appear before fracture interference occurs and compound linear flow (late linear flow) arises after fractures start to interfere with each other. At last, the boundary-dominated flow (pseudosteady-state flow) happens in the middle and late production period. Except for the early linear flow, other flow regimes are similar in all three fracture-geometry scenarios. In this study, the flow regimes for complex fractures include compound linear flow, early radial flow, and pseudosteady-state flow (dominated by a closed reservoir boundary), whereas for the biwing fractures, the flow regimes consist of pseudolinear flow, early radial flow, compound linear flow, and pseudosteady-state flow (dominated by a closed boundary). In summary, their dominant flow regimes are linear flow and radial flow in the early period and pseudosteady-state flow in the middle and late production period.

Conclusions

1. Three fracture geometries—simple planar fractures, branching fractures, and a fracture network—are simulated in this study. All three scenarios have the same fracture volume and are all confined by the same microseismic-mapping data, and it is found that commonly used simple planar fractures overestimate the well productivity if a complex fracture network is created in the reservoir. The differences increase as the fracture conductivity increases. On the other hand, as geometry of fractures becomes more complex, the computational time increases.
2. For the ideal biwing fractures, main-fracture conductivity plays an essential role in the early period, while fracture half-length can significantly affect the long-term production. For different fracture geometries, the early production is similar (e.g., cumulative production of the first 6 months) and the differences arise around the end of the first year. The differences of complex fracture and ideal biwing fracture become large as the fracture conductivity increases.
3. Conductivity of the secondary fracture plays an important role on the post-stimulation well productivity. Secondary fractures with low conductivity can decrease the well productivity compared with wells with biwing planar fractures.
4. If a fracture network is intended to be created in the reservoir, especially at the presence of natural fractures, efforts must be made to achieve high conductivity of the secondary fractures. Under such circumstances, adding some complexity to the fracture geometry can increase well production (e.g., Scenario 2 under the conductivity ratio of 1:2), which is caused by a larger contact area between matrix and fracture. However, even with high secondary-fracture conductivity, a complicated fracture geometry (Scenario 3) still leads to a low long-term production. This is because of the shortened length of the main fracture.
5. Linear flow and radial flow (or elliptical flow) are dominant flow regimes in the early period, and pseudosteady-state flow is the most important regime in the middle and late periods. The flow regimes are similar between ideal biwing fractures and fractures with complexity, except the difference in early linear flow (i.e., compound linear flow arising in complex fractures and pseudolinear flow appearing in ideal biwing fractures).

Nomenclature

k_e = permeability of pseudoized fracture block in simulation model, darcies
K_f = permeability of hydraulic fracture, darcies
$q(t)$ = oil-production rate, STB/D
$Q(t)$ = cumulative oil production, STB
RNP = rate-normalized pressure, psi·D/STB
t_e = material-balance time, days
W_{block} = width of pseudoized fracture block in simulation model, m
W_f = width of hydraulic fracture, m

Acknowledgements

The authors gratefully acknowledge funding through a Discovery Grant from the Natural Sciences and Engineering Research Council of Canada and a Seed Grant from the University of Calgary to Shengnan Chen.

References

Bazan, L. W., Brinzer, B. C., Meyer, B. R. et al. 2013. Key Parameters Affecting Successful Hydraulic Fracture Design and Optimized Production in Unconventional Wells. Presented at the SPE Eastern Regional Meeting, Pittsburgh, Pennsylvania, USA, 20–22 August. SPE-165702-MS. http://dx.doi.org/10.2118/165702-MS.

Bear, J. 1972. *Dynamics of Fluids in Porous Media*, first edition. New York: Environmental Science Series, American Elsevier Publishing Company, Inc. 125–129.

Blick, E. F. and Civan, F. 1988. Porous-Media Momentum Equation for Highly Accelerated Flow. *SPE Res Eng* **3** (03): 1048–1052. SPE-16202-PA. http://dx.doi.org/10.2118/16202-PA.

Cipolla, C. L., Warpinski, N. R., Mayerhofer, M. J. et al. 2008. The Relationship Between Fracture Complexity, Reservoir Properties, and

Fracture Treatment Design. Presented at the SPE Annual Technical Conference and Exhibition, Denver, 21–24 September. SPE-115769-MS. http://dx.doi.org/10.2118/115769-MS.

Clarkson, C. R. 2013a. Production Data Analysis of Unconventional Gas Wells: Review of Theory and Best Practices. *Int J Coal Geol* **109–110** (April 2013): 101–146. http://dx.doi.org/10.1016/j.coal.2013.01.002.

Clarkson, C. R. 2013b. Production Data Analysis of Unconventional Gas Wells: Workflow. *Int J Coal Geol* **109–110** (April 2013): 147–157. http://dx.doi.org/10.1016/j.coal.2012.11.016.

CMG, 2013. IMEX User Manual. Calgary. Alberta: Computer Modeling Group Ltd.

Cooke, M. L. and Underwood, C. A. 2001. Fracture Termination and Step-Over at Bedding Interfaces Due to Frictional Slip and Interface Opening. *J Struct Geol* **23** (2–3): 223–238. http://dx.doi.org/10.1016/S0191-8141(00)00092-4.

Dahi Taleghani, A. and Olson, J. E. 2014. How Natural Fractures Could Affect Hydraulic-Fracture Geometry. *SPE Journal* **19** (01): 161–171. SPE-167608-PA. http://dx.doi.org/10.2118/167608-PA.

Fan, L., Thompson, J. W., and Robinson, J. R. 2010. Understanding Gas Production Mechanism and Effectiveness of Well Stimulation in the Haynesville Shale Through Reservoir Simulation. Presented at the Canadian Unconventional Resources and International Petroleum Conference, Calgary, 19–21 October. http://dx.doi.org/10.2118/136696-MS.

Fischer, T., Hainzl, S., Eisner, L. et al. 2008. Microseismic Signatures of Hydraulic Fracture Growth in Sediment Formations: Observations and Modeling. *Journal of Geophysical Research: Solid Earth* **113** (B2): B02307. http://dx.doi.org/10.1029/2007jb005070.

Ghaderi, S. M., Clarkson, C. R., and Kaviani, D. 2011. Investigation of Primary Recovery in Tight Oil Formations: A Look at the Cardium Formation, Alberta. Presented at the Canadian Unconventional Resources Conference, Calgary, 15–17 November. SPE-148995-MS. http://dx.doi.org/10.2118/148995-MS.

Ghaderi, S. M., Clarkson, C. R., and Kaviani, D. 2012. Evaluation of Recovery Performance of Miscible Displacement and WAG Processes in Tight Oil Formations. Presented at the SPE/EAGE European Unconventional Resources Conference and Exhibition, Vienna, Austria, 20–22 March. SPE-152084-MS. http://dx.doi.org/10.2118/152084-MS.

Hassanizadeh, S. M. and Gray, W. G. 1987. High Velocity Flow in Porous Media. *Transport Porous Media* **2** (6): 521–531. http://dx.doi.org/10.1007/bf00192152.

Iwere, F. O., Heim, R. N., and Cherian, B. V. 2012. Numerical Simulation of Enhanced Oil Recovery in the Middle Bakken and Upper Three Forks Tight Oil Reservoirs of the Williston Basin. Presented at the SPE Americas Unconventional Resources Conference, Pittsburgh, Pennsylvania, USA, 5–7 June. http://dx.doi.org/10.2118/154937-MS.

Kabir, S., Rasdi, F., and Igboalisi, B. 2011. Analyzing Production Data From Tight Oil Wells. *J Can Pet Technol* **50** (05): 48–58. SPE-137414-PA. http://dx.doi.org/10.2118/137414-PA.

Krause, F. F., Deutsch, K. B., Joiner, S. D. et al. 1994. Cretaceous Cardium Formation of the Western Canada Sedimentary Basin. In *Geological Atlas of the Western Canada Sedimentary Basin*. Canadian Society of Petroleum Geologists and the Alberta Research Council, http://www.ags.gov.ab.ca/publications/wcsb_atlas/a_ch23/ch_23.html (accessed 13 April 2015).

Legrand, N., De Kok, J., Neff, P. et al. 2011. Recovery Mechanisms and Oil Recovery From a Tight, Fractured Basement Reservoir, Yemen. *SPE Res Eval & Eng* **14** (04): 473–484. SPE-133086-PA. http://dx.doi.org/10.2118/133086-PA.

Liu, X., Zhou, Z., Li, X. et al. 2006. Understanding Hydraulic Fracture Growth in Tight Oil Reservoirs by Integrating Microseismic Mapping and Fracture Modeling. Presented at the International Oil & Gas Conference and Exhibition in China, Beijing, 5–7 December. SPE-102372-MS. http://dx.doi.org/10.2118/102372-MS.

Mageau, L., Zack, K., Bouchard, J. et al. 2012. Assessing the Cardium's Second Generation - A Look at Horizontal Well Performance by Area Raymond James Ltd, Vancouver, British Columbia, Canada (June 19, 2012). http://www.raymondjames.ca/en_ca/equity_capital_markets/equity_research/sample_research/docs/Junior%20Oil%20&%20Gas%20Producers.pdf.

Mayerhofer, M. J., Lolon, E., Warpinski, N. R. et al. 2008. What is Stimulated Rock Volume? Presented at the SPE Shale Gas Production Conference, Fort Worth, Texas, USA, 16–18 November. SPE-119890-MS. http://dx.doi.org/10.2118/119890-MS.

Mohammad, N. A. and Miskimins, J. 2012. A Comparison of Hydraulic-Fracture Modeling With Downhole and Surface Microseismic Data in a Stacked Fluvial Pay System. *SPE Prod & Oper* **27** (03): 253–264. SPE-134490-PA. http://dx.doi.org/10.2118/134490-PA.

Palisch, T., Duenckel, R., Bazan, L. et al. 2007. Determining Realistic Fracture Conductivity and Understanding Its Impact on Well Performance—Theory and Field Examples. Presented at the SPE Hydraulic Fracturing Technology Conference, College Station, Texas, 29–31 January. SPE-106301-MS. http://dx.doi.org/10.2118/106301-MS.

Potluri, N., Zhu, D., and Hill, A. D. 2005. The Effect of Natural Fractures on Hydraulic Fracture Propagation. Presented at the SPE European Formation Damage Conference, Sheveningen, The Netherlands, 25–27 May. SPE-94568-MS. http://dx.doi.org/10.2118/94568-MS.

Priyantoro, T. A., Prakoso, N. F., and Kahfie, R. M. 2012. Journey of Hydraulic Fracturing Improvement to Increase Oil Recovery from Sandstone Formation in Rimau Block. Presented at the SPE International Production and Operations Conference & Exhibition, Doha, 14–16 May. SPE-156550-MS. http://dx.doi.org/10.2118/156550-MS.

Quirk, D. J., Ziarani, A. S., Mills, S. T. et al. 2012. Integration of Microseismic Data, Fracture and Reservoir Simulation into the Development of Fractured Horizontal Wells in the Cardium Formation - A Tight Oil Case Study. Presented at the SPE Annual Technical Conference and Exhibition, San Antonio, Texas, USA, 8–10 October. SPE-160002-MS. http://dx.doi.org/10.2118/160002-MS.

Rubin, B. 2010. Accurate Simulation of Non Darcy Flow in Stimulated Fractured Shale Reservoirs. Presented at the SPE Western Regional Meeting, Anaheim, California, USA, 27–29 May. SPE-132093-MS. http://dx.doi.org/10.2118/132093-MS.

Siavoshi, J. and Bahrami, H. 2013. Interpretation of Reservoir Flow Regimes and Analysis of Welltest Data in Hydraulically Fractured Unconventional Oil and Gas Reservoirs. Presented at the SPE Unconventional Gas Conference and Exhibition, Muscat, Oman, 28–30 January. http://dx.doi.org/10.2118/164033-MS.

Song, B. and Ehlig-Economides, C. A. 2011. Rate-Normalized Pressure Analysis for Determination of Shale Gas Well Performance. Presented at the North American Unconventional Gas Conference and Exhibition, The Woodlands, Texas, USA, 14–16 June. SPE-144031-MS. http://dx.doi.org/10.2118/144031-MS.

Stalgorova, K. and Mattar, L. 2012. Practical Analytical Model To Simulate Production of Horizontal Wells With Branch Fractures. Presented at the SPE Canadian Unconventional Resources Conference, Calgary, 30 October–1 November. SPE-162515-MS. http://dx.doi.org/10.2118/162515-MS.

Stalgorova, K. and Mattar, L. 2013. Analytical Model for Unconventional Multifractured Composite Systems. *SPE Res Eval & Eng* **16** (03): 246–256. SPE-162516-PA. http://dx.doi.org/10.2118/162516-PA.

Varga, R. M., Stewart, R. R., and Bancroft, J. C. 2007. Inversion And Interpretation of Multicomponent Seismic Data: Willesden Green, Alberta. Presented at the 2007 SEG Annual Meeting, San Antonio, Texas, USA, 23–28 September. SEG-2007-1943.

Wang, Y., Yan B., and Killough, J. 2013 Compositional Modeling of Tight Oil Using Dynamic Nanopore Properties. Presented at the SPE Annual Technical Conference and Exhibition, 30 September–2 October, New Orleans, Louisiana, USA. SPE-166267-MS. http://dx.doi.org/10.2118/166267-MS.

Woo, V., Pope, T. L., Abou-khalil, E. et al. 2011. Fracture Stimulation Optimization in Horizontal Cardium Completions. Presented at the Canadian Unconventional Resources Conference, Calgary, 15–17 November. SPE-146785-MS. http://dx.doi.org/10.2118/146785-MS.

Menglu Lin is an MSc degree candidate in the Department of Chemical and Petroleum Engineering at the University of Calgary. His current research interests include rate-transient analysis, reserves evaluation, and reservoir modelling and simulation. Lin holds a BS degree in petroleum engineering from the China University of Geosciences. He is a member of SPE.

Shengnan Chen is an assistant professor in the Department of Chemical and Petroleum Engineering at the University of Calgary. Previously, she worked for 2 years as a consultant at

Enhanced Hydrocarbon Recovery Incorporated. Chen's major interests include unconventional-reservoir development, carbon dioxide enhanced oil recovery and storage, reservoir simulation, and optimization. She has authored or coauthored more than 30 technical papers. Chen holds BSc and MSc degrees in petroleum engineering from the China University of Petroleum and a PhD degree in petroleum systems engineering from the University of Regina. She is a member of SPE.

Wei Ding is a petroleum engineer in the Research Institute of Petroleum Exploration & Development (RIPED). His research interests include coalbed-methane development, horizontal wells, and reserves evaluation. Ding holds BSc and MSc degrees in petroleum engineering from the China University of Petroleum and a PhD degree from RIPED.

Zhangxin Chen is a professor in the Department of Chemical and Petroleum Engineering, currently holds the NSERC/AI-EES/Foundation CMG Industrial Research Chair in Reservoir Simulation and Alberta Innovates—Technology Futures Industrial Chair in Reservoir Modeling, and is director of the iCentre for Simulation & Visualization at the University of Calgary. His research interest is in petroleum engineering and numerical reservoir simulation for conventional and unconventional oil and gas reservoirs. Chen holds a PhD degree in reservoir simulation from Purdue University.

Jinze Xu has more than 3 years' experience in reservoir engineering in the petroleum industry. His research interest focuses on reservoir simulation in unconventional reservoirs. Xu holds a Masters of Science degree from the University of Calgary.